Investigation Study of Multi-Mode Multi-Speed Operation Method for Surface-Mounted Permanent Magnet Synchronous Machines

STANISLAV SIN[1], **MUHAMMAD AYUB**[1,2],
AND BYUNG-IL KWON[1], **(Senior Member, IEEE)**
[1]Department of Electrical and Electronic Engineering, Hanyang University, Ansan 15588, South Korea
[2]Department of Electronic Engineering, BUITEMS, Quetta 87650, Pakistan

Corresponding author: Byung-Il Kwon (bikwon@hanyang.ac.kr)

ABSTRACT Typically, a surface-mounted permanent magnet synchronous machine (SPMSM) has a poor flux-weakening performance due to its low synchronous inductance; hence, its speed is proportional to the supply voltage. A relatively high DC-link voltage is required to operate an SPMSM at higher speeds. This paper proposes a multi-mode multi-speed operation method to overcome this issue. With this method, the total line-to-line back electromotive force (EMF) is modified using the winding switching. Each phase of the stator winding is divided into two equal coils. There are four modes of operation of the machine. In mode I, the three-phase stator winding is connected in a wye configuration. In modes II, III, and IV, the winding is reconfigured such that the sum of the individual back EMFs of the coils exhibits a difference in voltages between the line terminals. The back EMF in these modes decreased by 1.74, 3.67, and 6.49 times, respectively, compared with that in mode I. This resulted in a four-speed operation, with base speeds of 1, 1.97, 3.68, and 7.47 pu in modes I–IV, respectively. Herein, the analytical model of the machine and drive topology are explained and demonstrated. Simulation results obtained using the 2-D finite element method are presented along with the experimental measurements to verify the feasibility of the proposed method.

INDEX TERMS Flux weakening, multi-speed operation, permanent magnet synchronous machine, winding configuration, winding switching.

LIST OF ABBREVIATIONS

Back EMF	Back electromotive force
BLDC	Brushless DC
CAD	Computer-aided design
CD	Circle diagram
FEA	Finite element analysis
FPGA	Field-programmable gate array
IGBT	Insulated-gate bipolar transistor
IPM machine	Interior permanent magnet machine
PID controller	Proportional–integral–derivative controller
pu	Per unit
PWM	Pulse-width modulation

LIST OF SYMBOLS

rms	Root mean square
SPMSM	Surface permanent magnet machine
E	Back EMF of a coil
E_U	Back EMF of phase U
E_{ll}	Line-to-line back EMF
I_{ch}	Characteristic current
I_d, I_q, I_0	Direct, quadrature, and zero components of current in the $dq0$ reference frame, respectively
I_U, I_V, I_W	Current in the corresponding phase
$I_{m\,ll}$	Rated line-to-line current
K	Field-weakening ratio
L_{aa}	Self-inductance of coil A
L_{ab}	Mutual inductance between coils A and B

L_d, L_q	Direct and quadrature components of inductance in the *dq0* reference frame, respectively
L_m, L_l	Magnetizing and leakage inductances of a coil, respectively
$L_{d\,ll}$	Line-to-line inductance
M	Phase mutual inductance
p	Number of pole pairs
R, R_a	Phase resistance and resistance of coil A, respectively
R_{ll}	Line-to-line resistance
T	Electromagnetic torque
V_d, V_q	Direct and quadrature components of voltage in the *dq0* reference frame, respectively
V_U	Voltages of phase U
V_{UV}	Voltage between lines U and V
$V_{m\,ll}$	Rated line-to-line voltage
α	Electrical angle between two coils
γ	Current angle referenced from the *q*-axis
δ	Current angle referenced from the *d*-axis
θ	Rotor angular position
λ	Flux linkage of a coil
λ_U	Flux linkage of phase U
$\lambda_{m\,ll}$	Line-to-line flux linkage
ω	Electrical angular frequency
ω_b, ω_m	Base rotational speed and maximal rotational speed, respectively

I. INTRODUCTION

During the early stages of the development of electrical machines, AC machines were regarded as constant-speed machines, which restricted their implementation. However, the development of power converters enabled the development of variable-speed drives based on AC machines. In recent times, most industrial applications have utilized these types of machines because of their reduced maintenance cost, robust structure, and efficiency.

Among AC machines, surface permanent magnet synchronous machines (SPMSMs) deliver a high torque per volume density and high efficiency with simple control techniques. Because of these advantages, SPMSMs continue to attract substantial interest.

When the machine is operated, the rotating magnetic field due to the permanent magnets induces a back electromotive force (EMF) opposing the current in the stator winding. The back EMF is proportional to the rotation speed; hence, at high speeds, excessive supply voltage is required to feed the stator winding current. At a certain speed, the machine reaches the supply voltage limit, and either an increased supply voltage or negative *d*-axis current I_d is necessary for counteracting the magnet flux. However, the supply voltage is often limited by the available DC-link voltage. On the other hand, the amount of flux that can be weakened by the negative current is proportional to the product of the synchronous inductance L_d and negative current I_d. Typically, I_d should not be greater than the machine-rated current. Furthermore, as an SPMSM

has an inherently low L_d, it exhibits an unsatisfactory flux-weakening performance [1]. It utilizes the magnetic torque exclusively; hence, the introduction of I_d does not produce a reluctance torque. Thus, the speed–torque capability curve of an SPMSM decreases quickly at speeds greater than the base speed.

Various methods have been proposed to improve the flux-weakening performance of SPMSMs. Fractional-slot concentrated windings have a high leakage inductance, which in combination with magnetizing inductance results in a higher overall L_d inductance, improving their constant-power operation [2], [3]. However, these windings result in a high degree of rotor losses [4] and unbalanced magnetic forces [5].

A more elegant approach is to place magnets inside the rotor to increase the synchronous inductance. Such machines are referred to as interior permanent magnet (IPM) machines. IPM machines also have a lower inductance along the *d*-axis than along the *q*-axis, which indicates that they can utilize both magnetic and reluctance torques. These features allow IPM machines to deliver a good flux-weakening performance over a wide range of speed [6]. Compared with SPMSMs, the disadvantages of these machines are their higher cost, complex manufacturing, and complicated controller structure.

It is also known that the back EMF value depends on the winding configuration. Consequently, winding switching has been proposed to reduce the induced back EMF and thus extend the operational speed. Numerous winding switching methods have been proposed. Among them, the most widely used methods are series/parallel switching [7], [8]; wye/delta switching [9], [10]; tapped winding switching [11], [12]; and cumulative/differential switching [14]–[20]. It is also possible to change the pole number via winding switching to improve the starting torque of line-start permanent magnet synchronous machines [21], [22].

In the cumulative/differential switching method, each phase is divided into two equal parts. Depending on the connection, the flux linkages of these parts aid or oppose each other, resulting in different phase-flux linkages. This method results in better speed extension compared with other methods. Moreover, it can still be combined with a conventional flux-weakening control by applying a negative I_d current [17]. However, this method requires an expensive dual-inverter topology [14]–[19].

In reference [20], a cumulative/differential machine operation that implemented winding switching for a single inverter was reported. This method achieved two-speed operation, and the back EMF in the differential mode was reduced 3.52 times compared with that in the cumulative mode. However, as it could be operated in only two discrete modes, its practical application was limited.

This paper proposes a modified winding switching scheme based on reference [20] to achieve a multi-mode multi-speed operation of an SPMSM. In this study, we combined the cumulative/differential and wye/delta switching methods. Thus, we can operate the machine in four modes, and the back
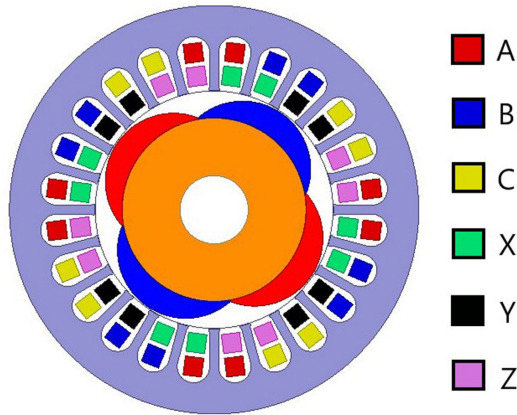
FIGURE 1. Cross section of the machine.

TABLE 1. Main machine parameters.

Parameter	Value
Stator outer diameter	120 mm
Rotor outer diameter	69 mm
Stack length	80 mm
Air gap length	0.5 mm
Magnet type	NdFeB
Residual flux density	1.2 T
Number of poles	4
Number of slots	24
Phase resistance	0.25 Ω

EMF can be reduced by up to 6.47 times. The four operation modes and increased speed range offer more flexibility in terms of practical application compared with [20], whereas the winding arrangement remains unchanged.

The remainder of this paper is organized as follows. The working principle and analytical model are described in Sections II and III, respectively. Additionally, we analyze the extension of the speed range through circle diagrams (CDs) in Section III. The simulation and experimental results of the low-power SPMSM are analyzed in Sections IV and V, respectively. The recently proposed winding switching methods are compared with the method proposed in this paper in Section VI. Finally, the paper is concluded and possible practical implementations of the proposed method are summarized in Section VII.

II. PROPOSED MULTI-MODE MULTI-SPEED OPERATION METHOD

The proposed operating method requires a special winding arrangement, which is described as follows: the machine is a 4-pole 24-slot SPMSM, with a three-phase winding having a coil pitch of five. The cross section of the machine is shown in Fig. 1, and its parameters are listed in Table 1. The stator winding has two layers: layer 1 is comprised of open-ended coils A, B, and C, spatially shifted between each other by $2\pi/3$ rad; layer 2 is comprised of open-ended coils X, Y, and Z, which are shifted by $\pi/6$ rad with respect to layer 1. Coils A, B, C, X, Y, and Z have an equal number of turns. The vector representation of the simplified machine is shown in Fig. 2.
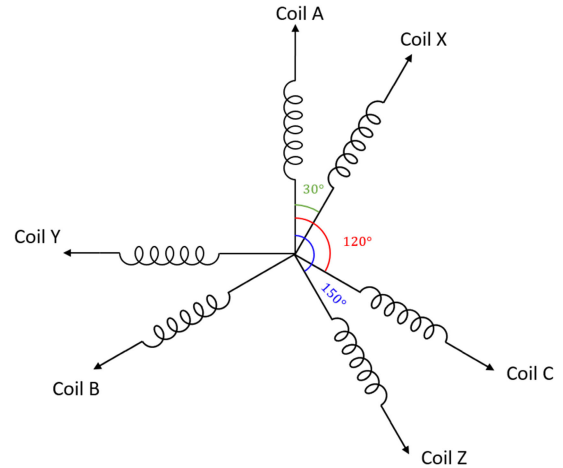

FIGURE 2. Simplified machine representation.

TABLE 2. Modes of the machine operation.

Mode	ON	OFF	E [pu]	T [pu]
Mode I	S1, S2, S3, S7, S8, S9	S4, S5, S6, S10, S11, S12	3.346	6.459
Mode II	S1, S2, S3, S10, S11, S12	S4, S5, S6, S7, S8, S9	1.932	3.730
Mode III	S4, S5, S6, S7, S8, S9	S1, S2, S3, S10, S11, S12	0.897	1.732
Mode IV	S4, S5, S6, S10, S11, S12	S1, S2, S3, S7, S8, S9	0.518	1

The machine is supplied by a well-established three-phase bridge inverter. The switching is realized through current bidirectional switches, which could be electric relays or power semiconductors such as antiparallel thyristors and transistors. The winding switching scheme is shown in Fig. 3(a); it has four modes of operation:

1. Cumulative wye – mode I (Fig. 3(b))
2. Cumulative delta – mode II (Fig. 3(c))
3. Differential wye – mode III (Fig. 3(d))
4. Differential delta – mode IV (Fig. 3(e))

The states of the switches for all the four modes and the corresponding back EMFs in per unit (pu) are listed in Table 2. Switches S1–S3 and S4–S6 should be turned on/off in a complementary manner, a rule that also applies to S7–S9 and S10–S12.

Mode I has the highest magnetic flux; therefore, its back EMF and torque will also be the highest. In this mode, the machine comprises a three-phase wye-connected winding with the following phases: phase U—coils A and X, phase V—coils B and Y, and phase W—coils C and Z. Considering a 30° shift and that all the coils have an equal number of turns, their line-to-line back EMF is as follows:

$$E_{ll1} = \sqrt{3}\left(E + Ee^{j30°}\right)e^{j30°} = 3.346Ee^{j45°}, \qquad (1)$$

where E_{ll1} is the line back EMF in mode I and E is the back EMF induced in a coil.

In (1), only the fundamental harmonic was considered. It is a good approximation for sinewave machines, as they are designed to have a negligible percentage of higher-order
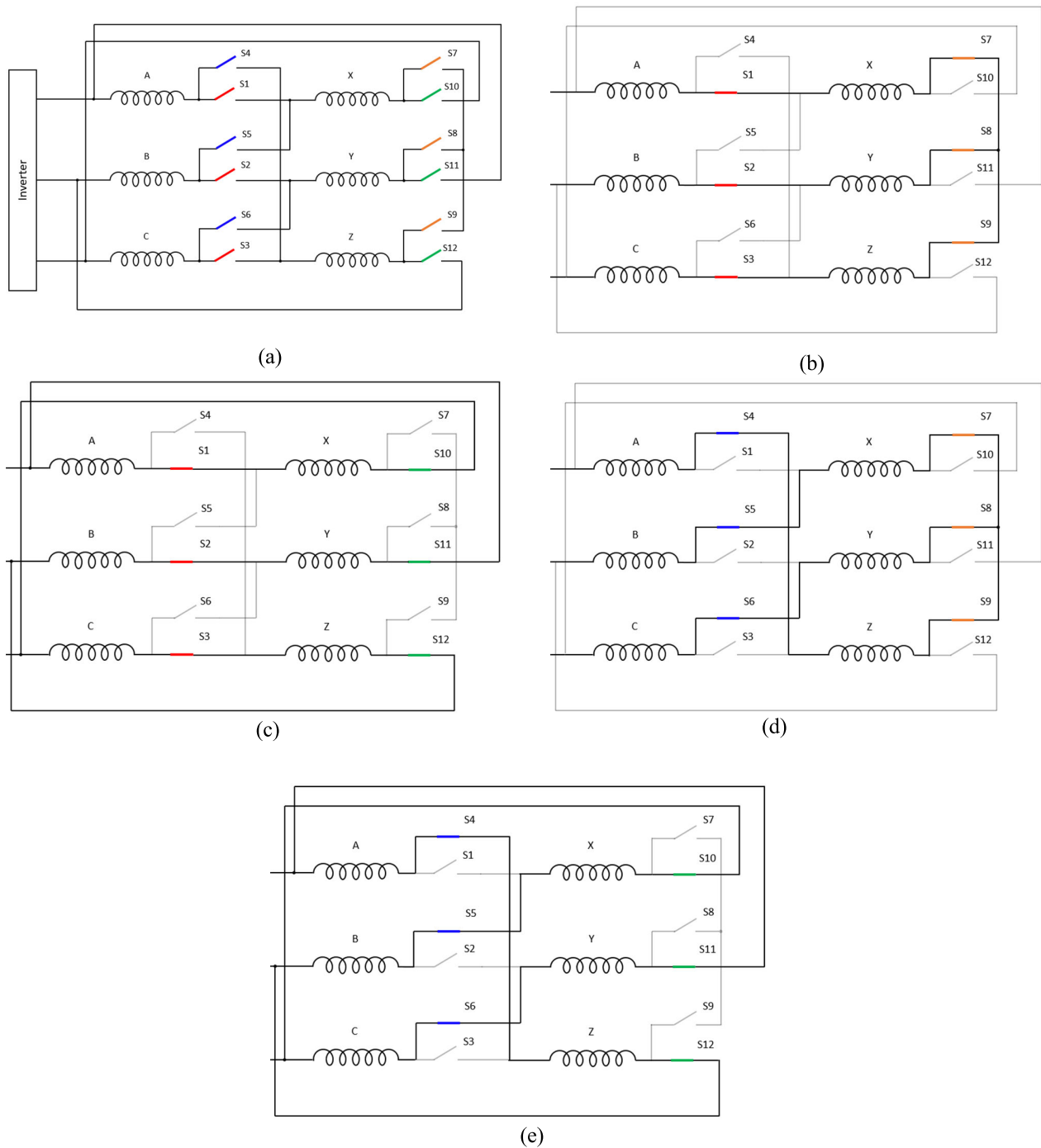
FIGURE 3. (a) Proposed winding switching scheme: (b) mode I, (c) mode II, (d) mode III, and (e) mode IV.

harmonics [23]. In square wave machines, these harmonics should be included in the calculations.

In mode II, the machine has the same phase composition as in mode I, but the windings are connected in a delta configuration. It is well known that the line back EMF will be reduced by $\sqrt{3}$ in delta mode; hence,

$$E_{ll2} = E + Ee^{j30°} = 1.932Ee^{j15°}. \quad (2)$$

In mode III, the machine has a wye-connected three-phase winding with the following phases: phase U—coils A and Z, phase V—coils B and X, and phase W—coils C and Y. Coils

A and Z are shifted by 150°; hence:

$$E_{ll3} = \sqrt{3}\left(E + Ee^{j150°}\right)e^{-j30°} = 0.897Ee^{j45°}. \quad (3)$$

In this mode, the back EMF is reduced by 3.73 times compared with that in mode I.

In mode IV, the phase composition of the machine is the same as in mode III; however, the windings are connected in a delta configuration. Hence, the line back EMF is reduced by $\sqrt{3}$. Thus,

$$E_{ll4} = E + Ee^{j150°} = 0.518Ee^{j75°} \quad (4)$$

Thus, this mode shows flux weakening by 6.46 times compared with that in mode I. Although modes III and IV show high flux weakening, they also introduce additional space harmonics. As will be shown in the next sections, the actual ratios differ slightly from the ones obtained in (3) and (4).

III. ANALYTICAL MODEL OF THE MACHINE

In this section, we will describe the development of the equivalent analytical model of the machine. We first describe the development of the inductances. Subsequently, the equations for the voltages and torques in each mode of the operation will be provided. Finally, the speed range will be analyzed using CDs.

Each layer has an equal number of turns and the magnetic path is almost the same; therefore, we can assume the self-inductances of layer 1 and layer 2 to be equal:

$$L_{aa} = L_{bb} = L_{cc} = L_{xx} = L_{yy} = L_{zz} = L_m + L_l, \quad (5)$$

where $L_{aa}, L_{bb}, L_{cc}, L_{xx}, L_{yy}, L_{zz}$ are the self-inductances of the corresponding coils, L_m is the magnetizing inductance, and L_l is the leakage inductance.

The mutual inductances between two coils can be calculated by

$$L_{nm} = L_m \cos(\alpha), \quad (6)$$

where L_{nm} is the mutual inductance, where the first letter of the subscript represents the affected coil, and the second letter represents the acting coil; α is the electrical angle between these coils.

From (6), the mutual inductances are

$$L_{ax} = L_{xa} = L_{by} = L_{yb} = L_{cz} = L_{zc} = L_m \cos(30°)$$
$$= \frac{\sqrt{3}}{2} L_m, \quad (7)$$

$$L_{ab} = L_{ba} = L_{bc} = L_{cb} = L_{ca} = L_{ac} = L_{xy} = L_{yx}$$
$$= L_{yz} = L_{zy} = L_{xz} = L_{zx} = L_m \cos(\pm 120°)$$
$$= -0.5 L_m, \quad (8)$$

$$L_{ay} = L_{ya} = L_{bz} = L_{zb} = L_{cx} = L_{xc} = L_m \cos(270°)$$
$$= 0, \quad (9)$$

$$L_{az} = L_{za} = L_{bx} = L_{xb} = L_{cy} = L_{yc} = L_m \cos(150°)$$
$$= -\frac{\sqrt{3}}{2} L_m. \quad (10)$$

Now, we can develop the equations of the flux linkages, voltages, and torque in each mode.

A. MODE I

The stator winding in mode I is shown in Fig. 3(b). Considering all the mutual inductances in this mode, the flux linkage of phase U is

$$\lambda_{U1} = (L_{aa} + L_{xx} + 2 * L_{ax}) I_U + (L_{ab} + L_{xb} + L_{ay} + L_{xy}) I_V$$
$$+ (L_{ac} + L_{xc} + L_{az} + L_{xz}) I_W + \lambda_m \sin(\omega t) + \lambda_m$$
$$\times \sin\left(\omega t + \frac{\pi}{6}\right), \quad (11)$$

where λ_{U1} is the flux linkage of phase U in mode; I_U, I_V, and I_W are the currents in phases U, V, and W, respectively; λ_m is the flux linkage of the magnets affecting a coil.

Using (7)–(10), we can simplify (11) as follows:

$$\lambda_{U1} = (3.732 L_m + 2L_l) \cdot I_U - 1.866 L_m \cdot I_V - 1.866 L_m \cdot I_W$$
$$+ 1.932 \lambda_m \sin\left(\omega t + \frac{\pi}{12}\right). \quad (12)$$

Note that the last term in (12) was calculated considering the imaginary and real parts. This term represents the back EMF induced in phase U. From (12), the equivalent inductances in mode I are

$$L_{U1} = 3.732 L_m + 2L_l, \quad (13)$$
$$M_1 = -1.866 L_m, \quad (14)$$
$$L_{d1} \approx L_{q1} = L_{U1} - M_1 = 5.598 L_m + 2L_l, \quad (15)$$

where L_{U1} and M_1 are the phase and mutual inductances in mode I, respectively; L_{d1} is the synchronous inductance, and L_{q1} is the quadrature inductance in mode I. The assumption is that $L_d = L_q$ is common for an SPMSM because the relative permeability of the magnet $\mu_r \approx 1$. Let us define the phase resistance as

$$R_a + R_x = R_b + R_y = R_c + R_z = R, \quad (16)$$

where $R_a, R_b, R_c, R_x, R_y, R_z$ are the resistances of the corresponding coils; R is the resistance of a phase.

We can now express the phase voltage equation for phase U as follows:

$$V_{U1} = (R_a + R_x) I_U + \frac{d\lambda_{U1}}{dt} = R \cdot I_U + (3.732 L_m + 2L_l)$$
$$\times \frac{dI_U}{dt} - (1.866 L_m) \frac{dI_V}{dt} - 1.866 L_m \frac{dI_W}{dt}$$
$$+ 1.932 \omega \lambda_m \cos\left(\omega t + \frac{\pi}{12}\right), \quad (17)$$

where V_{U1} is the phase voltage of phase U in mode I.

Let us define the back EMF as

$$E_{U1} = 1.932 \omega \lambda_m \cos\left(\omega t + \frac{\pi}{12}\right). \quad (18)$$

Performing a similar procedure for phases V and W, we obtain the matrix form of the phase voltages:

$$\begin{bmatrix} V_{U1} \\ V_{V1} \\ V_{W1} \end{bmatrix} = R \begin{bmatrix} I_U \\ I_V \\ I_W \end{bmatrix}$$
$$+ \begin{bmatrix} 3.732 L_m + 2L_l & -1.866 L_m & -1.866 L_m \\ -1.866 L_m & 3.732 L_m + 2L_l & -1.866 L_m \\ -1.866 L_m & -1.866 L_m & 3.732 L_m + 2L_l \end{bmatrix}$$
$$\times \frac{d}{dt} \begin{bmatrix} I_U \\ I_V \\ I_W \end{bmatrix} + \begin{bmatrix} E_{U1} \\ E_{V1} \\ E_{W1} \end{bmatrix}. \quad (19)$$

The torque can be calculated using the following equation:

$$T_1 = \frac{3}{2} p \cdot 1.932 \lambda_m I_s \sin\delta, \quad (20)$$

where T_1 is the torque in mode I, p the number of pole pairs, I_s is the line current, and δ is the current angle referenced from the d-axis.

It is well known that the line-to-line voltage in a wye-connected winding is obtained by multiplying the module of the phase voltage by $\sqrt{3}$. Considering the winding connection, the voltage between terminals U and V is shifted by 30° from the phase voltage V_{U1}.

$$V_{UV1} = V_{U1} - V_{V1} = \sqrt{3}V_{U1} \cdot e^{j30°}, \tag{21}$$

where V_{UV1} is the line voltage between terminals U and V in mode I.

The line-to-line resistance and inductance are expressed, respectively, as follows:

$$R_{ll1} = 2R, \tag{22}$$

$$L_{d\,ll1} = 2L_{d1} = 11.192L_m + 4L_l, \tag{23}$$

where R_{ll1} and $L_{d\,ll1}$ are the line resistance and line synchronous inductance, respectively, in mode I.

B. MODE II

The machine in mode II is shown in Fig. 3(c). The connection has been changed from wye to delta. Therefore, (11)–(21) are valid for this mode as well. However, the line voltage between terminals U and V is

$$V_{UV2} = -V_{V2}. \tag{24}$$

The line resistance and inductance are now expressed, respectively, as

$$R_{ll2} = \frac{2}{3}R, \tag{25}$$

$$L_{d\,ll2} = \frac{2}{3}L_{d1} = 3.731L_m + \frac{4}{3}L_l. \tag{26}$$

Equations (24)–(26) show that the line voltages decreased by 1.732 times, whereas the resistances and inductances decreased by 3 times. Applying Kirchhoff's current law in this mode, we determine that line current is greater than the phase current by 1.732 times.

Finally, the torque is expressed as

$$T_2 = \frac{\sqrt{3}}{2}p \cdot 1.932\lambda_m I_s sin\delta = \frac{T_1}{\sqrt{3}}. \tag{27}$$

As shown in (27), the torque in mode II is lower than that in mode I by $\sqrt{3}$ times for the same line current.

C. MODE III

The machine in mode III is shown in Fig. 3(d). As the winding composition has changed, we need to modify (7)–(16) according to the new connection.

The flux linkage is expressed as

$$\lambda_{U3} = (L_{aa}+L_{zz}+2*L_{az})\,I_U + (L_{ab}+L_{zb}+L_{ax}+L_{zx})\,I_V$$
$$+ \left(L_{ac}+L_{zc}+L_{ay}+L_{zy}\right)I_W + \lambda_m \sin(\omega t) + \lambda_m$$
$$\times \sin\left(\omega t + \frac{5\pi}{6}\right), \tag{28}$$

$$\lambda_{U3} = (0.268L_m+2L_l) \cdot I_U - 0.134L_m \cdot I_V - 0.134L_m$$
$$\cdot I_W + 0.518\lambda_m \times \sin\left(\omega t + \frac{5\pi}{12}\right), \tag{29}$$

Note that the term λ_m decreases by 3.73 times compared with that in (20). This results in a decreased back EMF and torque.

Hence, the inductances in mode III are

$$L_{U3} = 0.268L_m + 2L_l, \tag{30}$$

$$M_3 = -0.134L_m, \tag{31}$$

$$L_{d3} \approx L_{q3} = L_{U3} - M_3 = 0.402L_m + 2L_l. \tag{32}$$

The synchronous inductance decreases compared with that in mode I. This results in a poorer flux-weakening capability by applying the negative I_d current in modes III and IV, compared with that in mode I.

The phase voltage and back EMF are expressed as

$$V_{U3} = R \cdot I_U + (0.268L_m+2L_l)\frac{dI_U}{dt} - 0.134L_m\frac{dI_V}{dt}$$
$$- 0.134L_m\frac{dI_W}{dt} + 0.518\omega\lambda_m cos\left(\omega t + \frac{5\pi}{12}\right), \tag{33}$$

$$E_{U3} = 0.518\omega\lambda_m cos\left(\omega t + \frac{5\pi}{12}\right). \tag{34}$$

The voltage equations are expressed as follows:

$$\begin{bmatrix} V_{U3} \\ V_{V3} \\ V_{W3} \end{bmatrix} = R\begin{bmatrix} I_U \\ I_V \\ I_W \end{bmatrix}$$
$$+ \begin{bmatrix} 0.268L_m+2L_l & -0.134L_m & -0.134L_m \\ -0.134L_m & 0.268L_m+2L_l & -0.134L_m \\ -0.134L_m & -0.134L_m & 0.268L_m+2L_l \end{bmatrix}$$
$$\times \frac{d}{dt}\begin{bmatrix} I_U \\ I_V \\ I_W \end{bmatrix} + \begin{bmatrix} E_{U3} \\ E_{V3} \\ E_{W3} \end{bmatrix}. \tag{35}$$

Similarly, the torque in this mode is

$$T_3 = \frac{3}{2}p \cdot 0.518\lambda_m I_s sin\delta. \tag{36}$$

Equation (36) shows that the torque is reduced by the same extent as the back EMF compared with the corresponding values in mode I.

The line-to-line parameters in mode III are

$$V_{UV3} = V_{U3} - V_{V3} = \sqrt{3}V_{U3} \cdot e^{j30°}, \tag{37}$$

$$R_{ll3} = 2R, \tag{38}$$

$$L_{d\,ll3} = 2L_{d3} = 0.804L_m + 4L_l. \tag{39}$$

D. MODE IV

The machine in mode IV is shown in Fig. 3(e); the winding composition is the same as in mode III. Therefore, (29)–(35) are valid for this mode as well. The line-to-line parameters are

$$V_{UV4} = V_{U4}, \tag{40}$$

$$R_{ll4} = \frac{2}{3}R, \tag{41}$$

$$L_{d\,ll4} = \frac{2}{3}L_{d3} = 0.268L_m + \frac{4}{3}L_l. \tag{42}$$

Finally, the torque is expressed as

$$T_4 = \frac{\sqrt{3}}{2}p \cdot 0.518\lambda_m I_s sin\delta = \frac{T_3}{\sqrt{3}}. \tag{43}$$
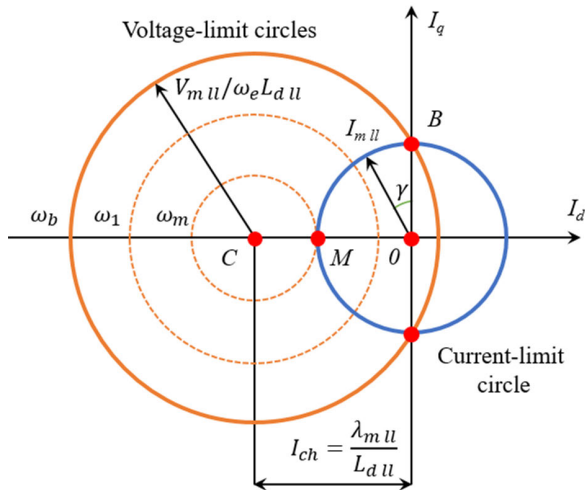
FIGURE 4. Circle diagram of the SPMSM.

E. SPEED RANGE ANALYSIS

In this subsection, we will analyze the speed range of the machine by using CDs. A CD is a powerful tool that provides a descriptive visual and simple explanation of the variable-speed operation of a machine. An example of such a diagram is shown in Fig. 4. In this figure, all the parameters are considered as line-to-line, $\omega_b < \omega_1 < \omega_m$, where ω is the rotational speed, and the subscripts b and m denote the base and maximal speeds, respectively.

We first perform the coordinate transformation to plot the CDs. The current equations in the *abc* reference frame can be transformed into the *dq0* synchronous reference frame using the Park transformation as follows:

$$\begin{bmatrix} I_d \\ I_q \\ I_0 \end{bmatrix} = \begin{bmatrix} I_a \\ I_b \\ I_c \end{bmatrix} \sqrt{\frac{2}{3}}$$

$$\times \begin{bmatrix} \cos(\theta) & \cos\left(\theta - \frac{2\pi}{3}\right) & \cos\left(\theta + \frac{2\pi}{3}\right) \\ \sin(\theta) & \sin\left(\theta - \frac{2\pi}{3}\right) & \sin\left(\theta + \frac{2\pi}{3}\right) \\ \frac{\sqrt{2}}{2} & \frac{\sqrt{2}}{2} & \frac{\sqrt{2}}{2} \end{bmatrix},$$

$$(44)$$

where θ is the rotor angular position.

This transformation simplifies the control of AC machines because all the space vectors are stationary with respect to the rotor.

Subsequently, the current-limit circle is plotted at the origin of the *dq* coordinates. The circle radius equals the magnitude of the machine line current. The current angle γ can be controlled by introducing different *d* and *q* currents. From (20), it is evident that the torque will be maximum at $\delta = 90°$. In other words, the condition for the maximum torque per ampere control is that only the *q*-axis component of the current exists, and its *d*-axis component is zero. It is convenient to align the current vector with the *q*-axis by defining $\gamma = 0$.

Now, the steady-state voltage equations can be expressed as

$$V_d = RI_d - \omega L_q I_q, \tag{45}$$

$$V_q = RI_q + \omega \left(\lambda_m + L_d I_d \right). \tag{46}$$

Let us denote the maximum line-to-line voltage as $V_{m\,ll}$. Then, neglecting the phase resistances, from (45) and (46), we obtain

$$V_{m\,ll} = \left(X_{qll} I_q \right)^2 + \left(E_q + X_{d\,ll} I_d \right)^2. \tag{47}$$

As mentioned previously, $L_d = L_q$ for the SPMSM; hence, (47) represents the circle of radius $V_{m\,ll}$, centered at point C $(0, -\lambda_{m\,ll}/L_{d\,ll})$. The term $\lambda_{m\,ll}/L_{d\,ll}$ is called the characteristic current I_{ch}. We can now plot a group of voltage-limit circles, as shown in Fig. 4. Note that the voltage-limit circle shrinks when the speed of the machine increases.

The base speed is defined as the maximum speed at which the rated torque can be maintained at a given supply voltage. The solid circle in Fig. 4 represents the voltage limit at the base speed, and the intersection of the voltage- and current-limit circles occurs at $\gamma = 0°$ (point B). From (47), we can calculate the base speed as follows:

$$\omega_b = \frac{1}{p} * \frac{V_{m\,ll}}{\sqrt{\lambda_{m\,ll}^2 + (L_{d\,ll} I_d)^2}}. \tag{48}$$

In an NdFeB SPMSM, the magnet flux is much higher than the inductance L_d. This typically results in a characteristic current several times greater than the rated current. If we neglect the second term of the denominator in (48), we obtain the simple dependence $\omega_b \approx V_{m\,ll}/p\lambda_{m\,ll}$. Hence, the base speed increase of the SPMSM in modes II–IV is inversely proportional to the flux of the magnets.

The smallest dashed circle represents the voltage limit at the maximal achievable speed ω_m. At this speed, $\gamma = 90°$ (point M) and the current $I_d = -I_{m\,ll}$. The ratio of the maximal speed to the base speed can be calculated as follows [24]:

$$\frac{\omega_m}{\omega_b} = \frac{\sqrt{s^2 + 1}}{s - 1}, \tag{49}$$

where *s* is the pu characteristic current $s = I_{ch}/I_{m\,ll}$.

If $I_{ch} \gg I_{m\,ll}$, then $\omega_m/\omega_b \approx 1$. This statement can be applied to modes II–IV because, as was shown in subsections IIIA–IIID, the normalized flux and synchronous inductance are related as follows:

$$K = \frac{\lambda_{m\,ll\,1}}{\lambda_{m\,ll\,x}} \approx \sqrt{\frac{L_{d\,ll1}}{L_{d\,llx}}}, \tag{50}$$

where *K* is the flux-weakening ratio and the subscript *x* denotes the number of the operation mode.

Equation (50) is evident from (15), (26), (32), and (39). Note that, in (50), the leakage component was neglected, as it is only a small percentage of L_d. Therefore, the characteristic current increases, and the voltage-limit circle moves to the left along the *d*-axis.
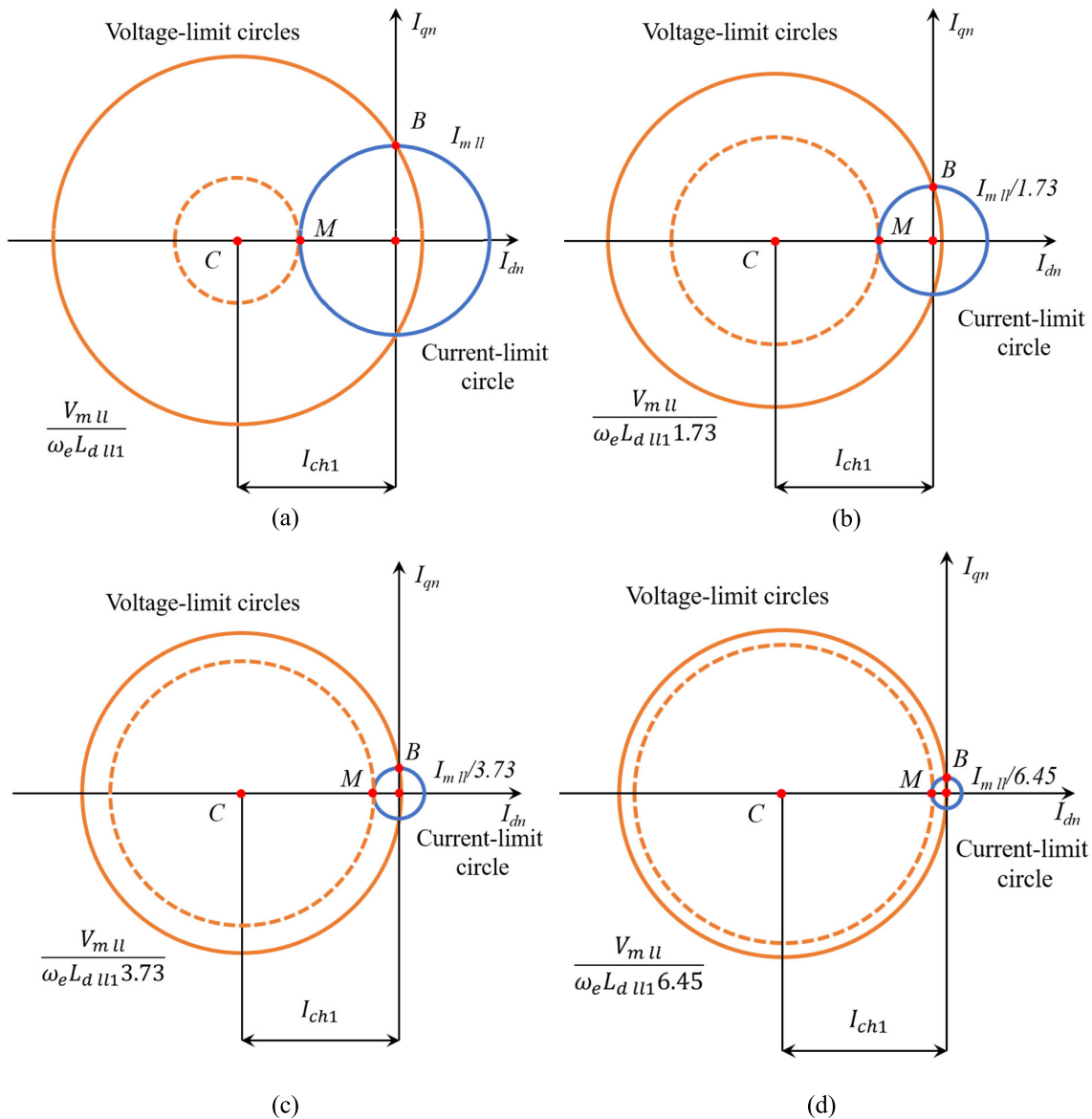
FIGURE 5. Normalized CDs: (a) mode I, (b) mode II, (c) mode III, and (d) mode IV.

For a convenient analysis, the CDs of the machine in the four modes of operation were normalized as shown in Figs. 5(a)–(d). All the quantities were divided by the flux-weakening ratio K, to demonstrate the torque drop and flux-weakening performance. When the mode is changed, the current terms decrease K times, the characteristic current remains unchanged, and the speed scale increases K times. The solid circles in Figs. 5(a)–(d) represent the voltage limits at the base speed, and the dashed circles show the limits at the maximum speed. The ratio ω_m/ω_b approaches unity in modes II–IV, as stated previously. Although the performance of the flux weakening using a negative d-current was degraded, the base speed of the machine increased noticeably because of the decrease in the effective magnet flux linkage.

The current and torque trajectories during the machine operation can be understood from Fig. 6. In this figure, there are four I_d, I_q planes for each operating mode, and each of

these planes has a different flux linkage; hence, the torques and achieved speeds are also different. The machine is started in mode I, and I_q is maintained at a maximum until the base speed is reached. Subsequently, the machine enters the flux-weakening region, and a negative I_d is applied to satisfy the voltage constraints. When the torque achieved in mode I is lower than the rated torque of mode II, the machine transits to the next operation plane. In the operation plane of mode II, the decreased flux linkage allows the machine to run until a certain speed, at the cost of decreased torque, as shown in the upper section of Fig. 6. This procedure is repeated until the maximum speed in mode IV.

IV. PERFORMANCE ANALYSIS USING 2-D FEA
A. STEADY-STATE ANALYSIS
A computer-aided design (CAD) model of the SPMSM with sinusoidal back EMF was used to verify the flux weakening
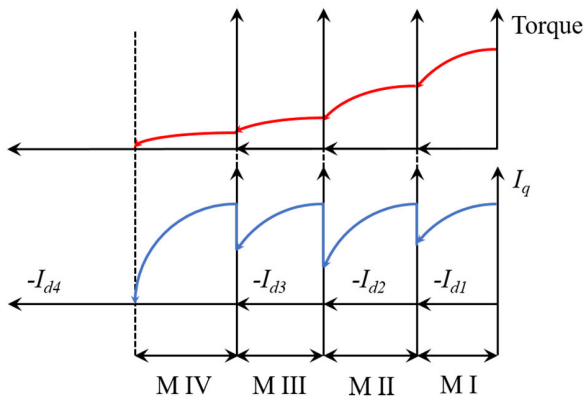
FIGURE 6. Current and torque trajectories during the machine operation.

calculated in (1)–(4). The same machine will be used later in the experiment. Its cross section is shown in Fig. 1 and its parameters are listed in Table 1. A fine sliding mesh was used to assure the correctness of the simulation results. The number of elements was 42832, and the minimal mean

element area was 7×10^{-7} mm^2. The vector potential boundary was set to zero at the outer surface of the stator.

First, the machine was simulated under a no-load condition at a base speed of 300 rpm to demonstrate the magnet flux linkages and back EMF. The line-to-line flux linkages in the four modes of operation are shown in Figs. 7(a)–(d). As evident from these figures, the rms values of the line flux linkages are 0.5834, 0.3367, 0.1567, and 0.0904 Wb in modes I–IV, respectively. The flux linkages in modes II–IV decreased by 1.733, 3.723, and 6.453 times compared with that in mode I, respectively.

The line back EMFs of the machine at 300 rpm are shown in Figs. 8(a)–(d), and their rms values are 36.6514, 21.1402, 9.8287, and 5.6623 V in modes I–IV, respectively. The back EMFs in modes II–IV decreased by 1.734, 3.729, and 6.473 times, respectively, compared with that in mode I. The back EMF was reduced by changing the winding configuration; hence, the speed of the machine could be increased further.

Subsequently, the machine was simulated at a rated load of 2.5 Arms and a speed of 300 rpm. The torques in the

(a)

(b)

(c)

(d)
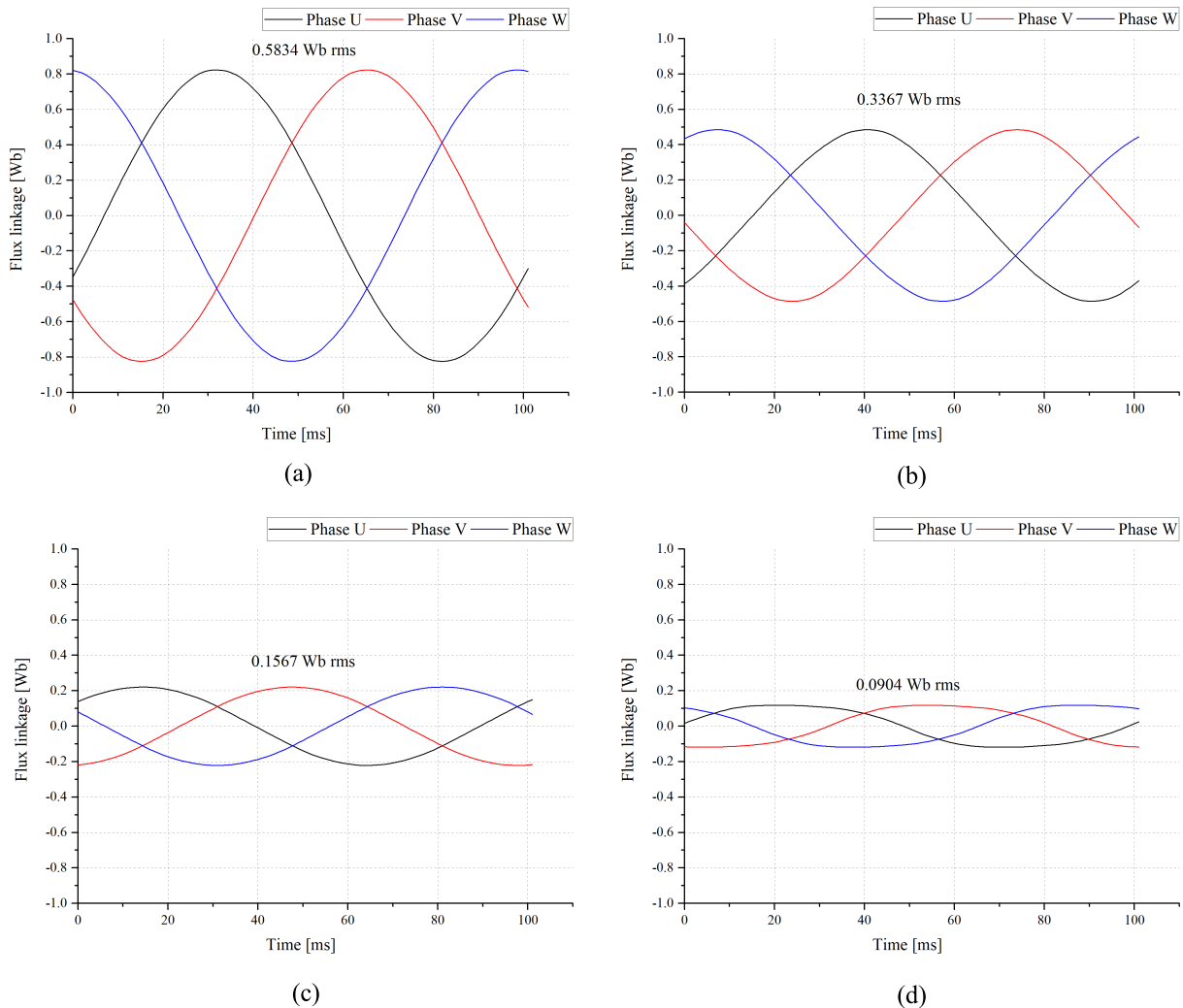
FIGURE 7. Flux linkage of the machine: (a) mode I, (b) mode II, (c) mode III, and (d) mode IV.
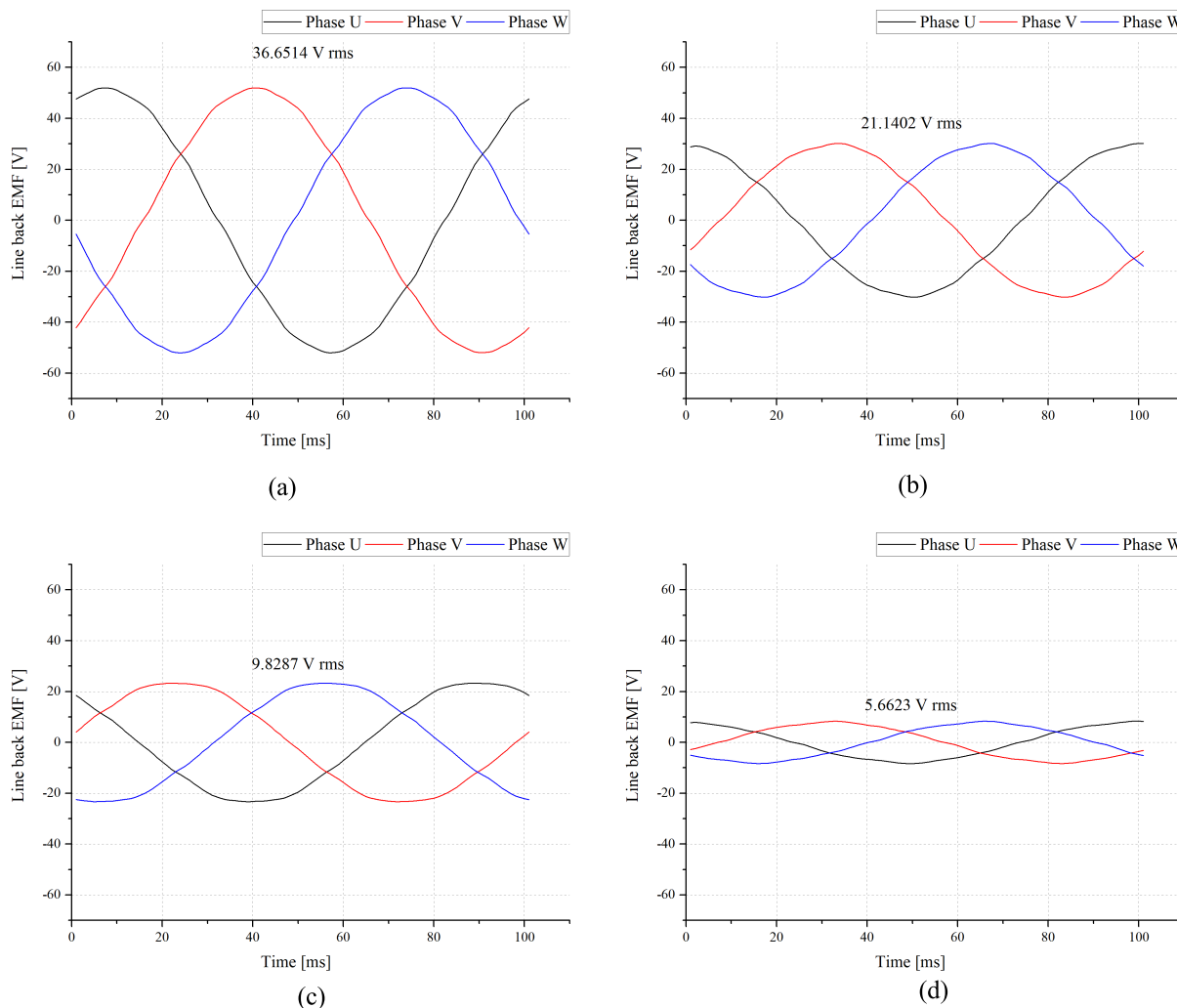
FIGURE 8. Back EMF of the machine: (a) mode I, (b) mode II, (c) mode III, and (d) mode IV.
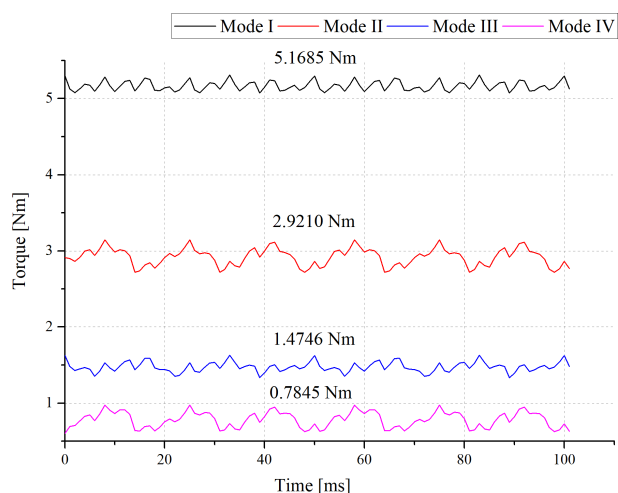

FIGURE 9. Torque of the machine at 300 rpm.

four modes are shown in Fig. 9. They were 5.1685, 2.9210, 1.4746, and 0.7845 Nm, respectively, in modes I–IV. The torques in modes II–IV decreased by 1.7694, 3.5050, and 6.5883 times, respectively, compared with that in mode I.

These results deviated slightly from the predicted values owing to some unwanted harmonics in the phase-to-phase back EMF.

The torque–speed curves of the machine are shown in Fig. 10. The base speeds were 300, 586, 1110, and 2208 rpm in modes I–IV, respectively. The rated powers were 162.3736, 179.2498, 171.4063, and 181.3935 W in modes I–IV, respectively.

B. TRANSIENT ANALYSIS

The abrupt rise in circuit voltage and/or current is a concern in all winding switching schemes. Thus, an appropriate switch control should be employed to minimize such voltage/current spikes.

As mentioned in section III, switch groups S1–S3 and S4–S6 should be switched in a complementary manner, as should groups S7–S9 and S10–S12. For example, turning on switches S1–S3 and S4–S6 simultaneously results in a short-circuit and, consequently, overcurrent. Turning off switches S1–S3 and S4–S6 simultaneously would force the winding current to decline instantly; as the voltage
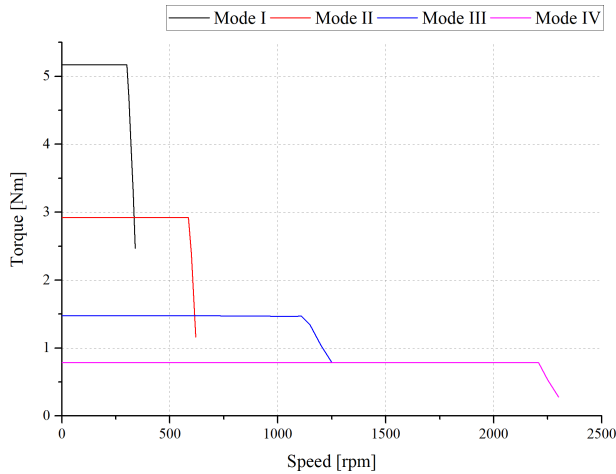
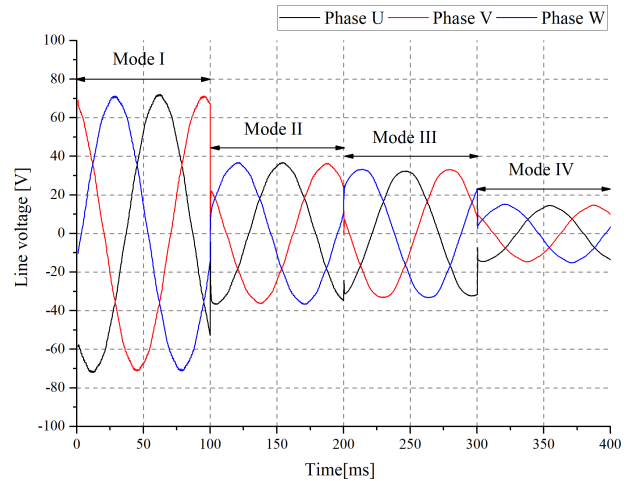**FIGURE 10.** Speed–torque capability curves of the machine.

FIGURE 11. Flowchart of the winding switching simulation.

FIGURE 12. Voltage applied to the machine in the four modes at 300 rpm.

FIGURE 13. Phase current transients.

drop is given by

$$V = RI + L\frac{dI}{dt}, \tag{51}$$

the last term in (51) would cause a large voltage spike.

To avoid this, the turn on/off delays should be carefully considered. However, modern IGBTs have superior switching delays of the order of a few microseconds; consequently, the switching delay can be ignored.

The winding was reconfigured according to Table 2 at the rated load and speed to demonstrate the machine transients. All the switches were turned on/off simultaneously. During the simulation, we made the following assumptions:

1. The speed during and after the reconfiguration remained constant.
2. The switching delay was ignored.
3. The power supply was simulated as a voltage source.

The flowchart of the winding switching simulation is shown in Fig. 11. The simulation was started in mode I, switches S1–S3 and S7–S9 were turned on, and the remaining switches were turned off. The voltage was calculated by the current controller based on the parameters of the basic three-phase machine. When the switching command was received, the states of switches S7–S9 and S10–S12 were inversed, and mode II was activated. Simultaneously, the required
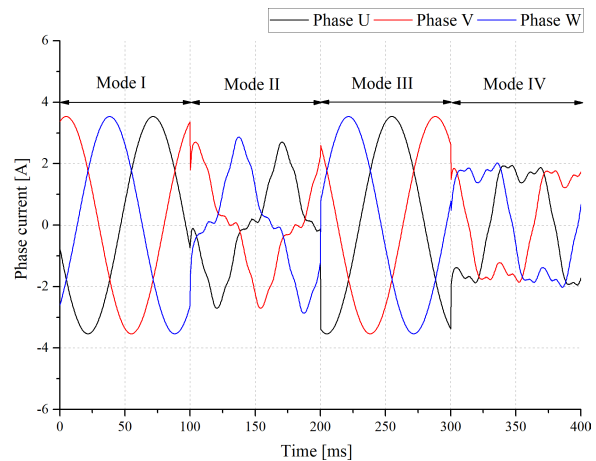
voltage was calculated according to the corresponding equations given in Section III. The zero reference of the rotor angular position was shifted because the back EMF angle had changed. The algorithm is similar for other reconfigurations. Consider that the turned on switches are S4–S9 for mode II and S4–S6 and S10–S12 for mode III.

The line voltage applied during the transitions is shown in Fig. 12. We reconfigured the winding from mode I to mode II at 100 ms, from mode II to mode III at 200 ms, and from mode III to mode IV at 300 ms.

The phase current transients are shown in Fig. 13. The line current was maintained at 2.5 A_{rms}, and hence, the phase current was $2.5/\sqrt{3} = 1.4434$ A_{rms} during the operation in modes II and IV.

The torque transients are shown in Fig. 14; as can be seen, the torque changes almost instantly after the winding switching. The torques in each mode have the same values as in Fig. 9.

The coil voltage transients are shown in Fig. 15. Here, although the voltage in the coils declined instantly, there was no significant voltage rise.
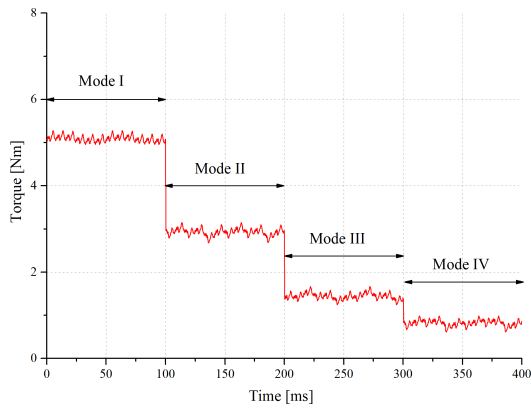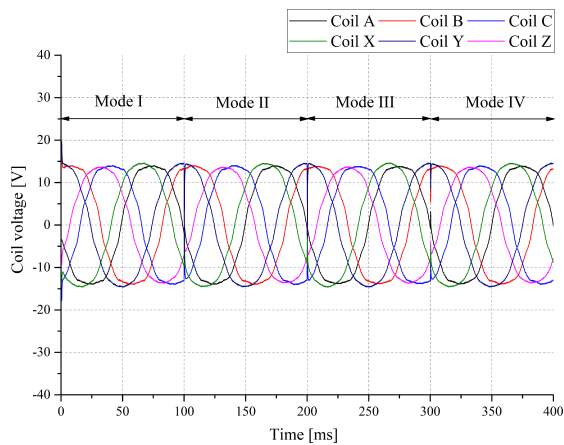
FIGURE 14. Torque transients.
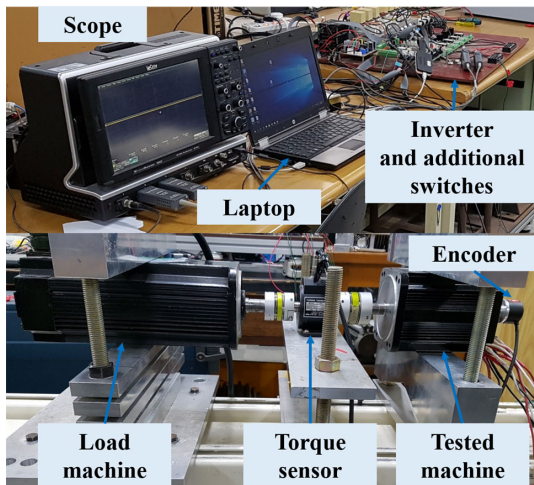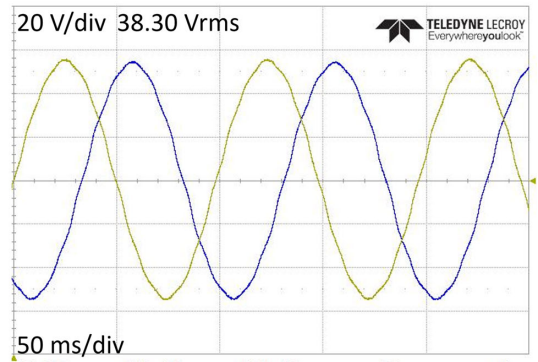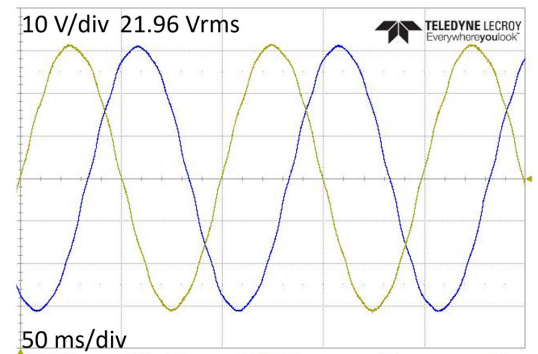

FIGURE 15. Coil voltage transients.

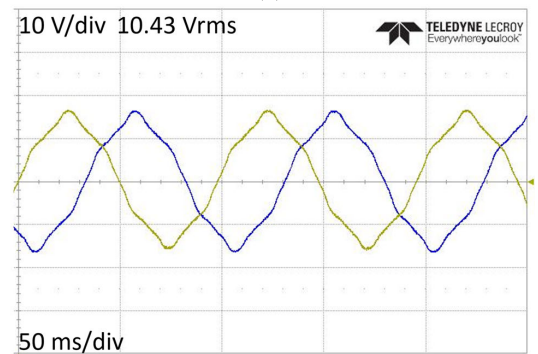**FIGURE 16.** Experimental setup.

V. EXPERIMENTAL RESULTS

The proposed multi-speed operation method was tested on a commercially available three-phase, 4-pole, 24-slotted SPMSM with a sinusoidal back EMF waveform. It was rewound as shown in Fig. 1 and the machine parameters are listed in Table 1. The machine was supplied by a custom-made three-phase inverter, which was controlled by a Texas Instruments TMS320F28335 microprocessor on an FPGA. SEMIKRON International IGBTs were used
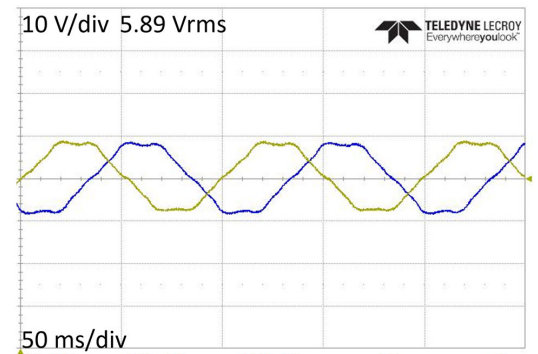

FIGURE 17. Measured back EMFs: (a) mode I; (b) mode II; (c) mode III; and (d) mode IV.

as inverters and additional switches. The rotary encoder E40S8 was used as a position sensor. The experimental setup is shown in Fig. 16.
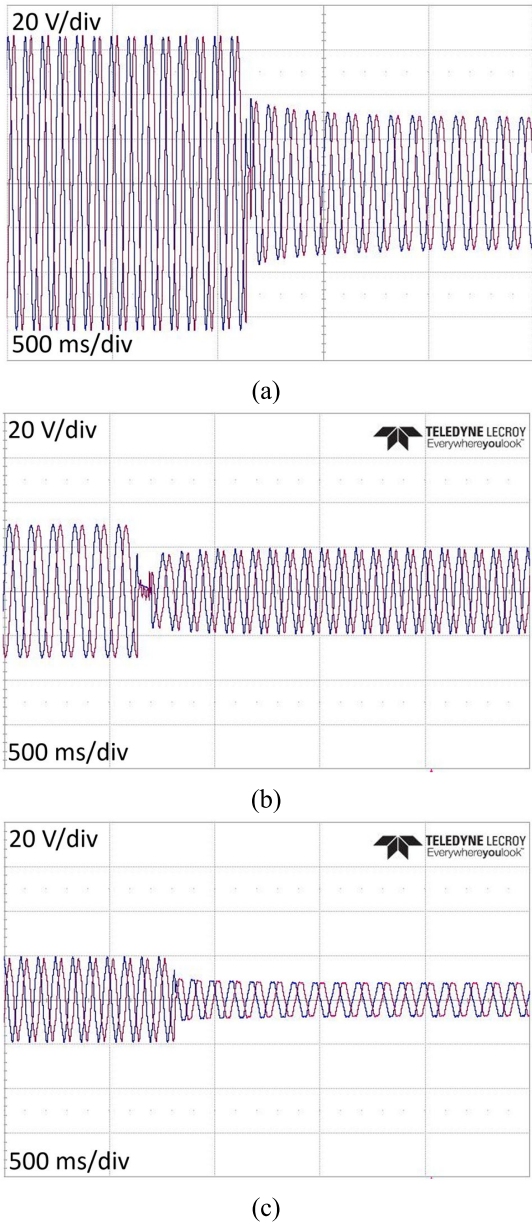
(a)

(b)

(c)

FIGURE 18. Measured back EMF transients: (a) from mode I to mode II, (b) from mode II to mode III, and (c) from mode III to mode IV.

A. NO-LOAD EXPERIMENT
Initially, the no-load experiments were performed to verify the weakening of the back EMF. The tested machine was connected to the prime mover, which was a two-pole three-phase induction machine. The line back EMFs were measured in the four modes of operation at 300 rpm, as shown in Figs. 17(a)–(d). The back EMFs were 38.30, 21.96, 10.43, and 5.90 V_{rms} in modes I–IV, respectively. Subsequently, the flux weakening with respect to mode I was 1.7440, 3.6721, and 6.4915 times, respectively, in modes II–IV.

Then, the no-load winding at the base speed was reconfigured from mode I to mode II, from mode II to mode III, and from mode III to mode IV. The measured back EMF transients are shown in Figs. 18(a)–(c), indicating that severe
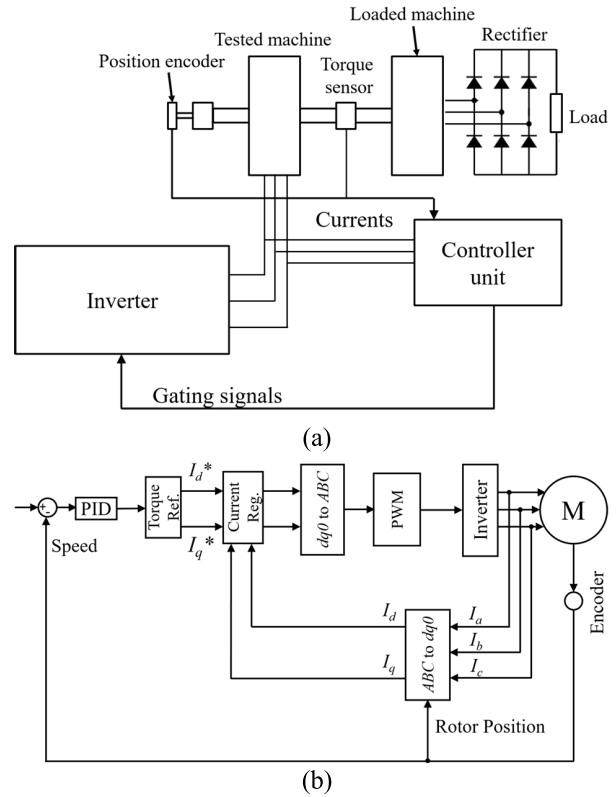

(a)

(b)

FIGURE 19. (a) Block diagram of the experimental setup for the loaded experiments. (b) Speed control unit.

voltage transients were avoided during the machine operation because the windings had been reconfigured at the no-load condition.

B. LOADED EXPERIMENT
The tested SPMSM was used as a prime mover for the load brushless DC (BLDC) machine to conduct the loaded experiments. The outputs of the BLDC machine were connected to the resistive loading through a three-phase bridge rectifier as shown in Fig. 19(a). The rated line current was 2.5 A_{rms}, and the machine was controlled using the speed control unit.

The speed control unit is shown in Fig. 19(b). The output current was transformed from the abc coordinate reference frame into the rotational *dq0* coordinate reference frame. The control unit calculated the reference I_d and I_q values, which were regulated by two proportional–integral–derivative (PID) controllers. Then, the *dq0* components of the voltage were transformed into the abc coordinate reference frame. Finally, the calculated voltages were fed to the pulse-width modulation (PWM) unit, which formed gating signals for the inverter.
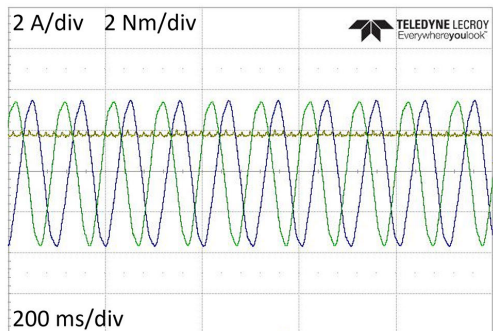
The torques of the machine at 300 rpm are shown in Fig. 20(a)–(d). They were 5.137, 2.899, 1.455, and 0.792 Nm in modes I–IV, respectively. It is evident that the torque declined proportionally to the reduced back EMF. The DC-link voltage was set to 103 V, and the modulation index was 0.8, which resulted in a line voltage of $103 \times 0.8/\sqrt{2} = 58.26$ V_{rms}.
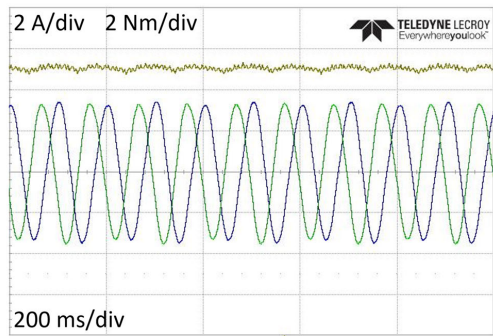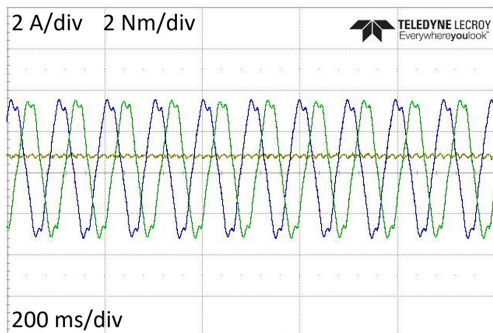
(a)
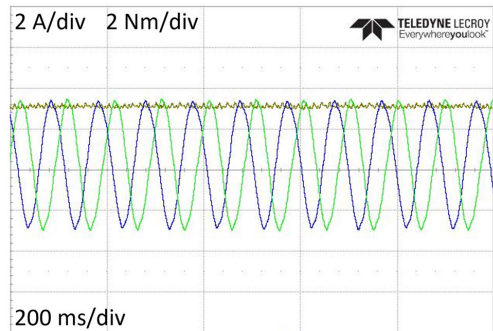
(b)

(c)

(d)

FIGURE 20. Measured torques at the rated loading and 300 rpm speed: (a) mode I, (b) mode II, (c) mode III, and (d) mode IV.

Subsequently, the winding reconfigurations were performed from mode I to mode III and from mode II to mode IV. The torque and current transitions are shown in Fig. 21(a)–(b). A dead time was introduced to avoid unacceptable transients. In Fig. 21(a), the controller settings and
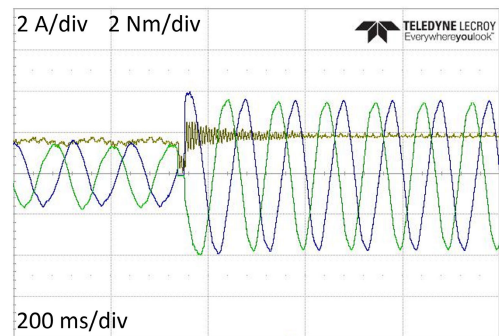
(a)
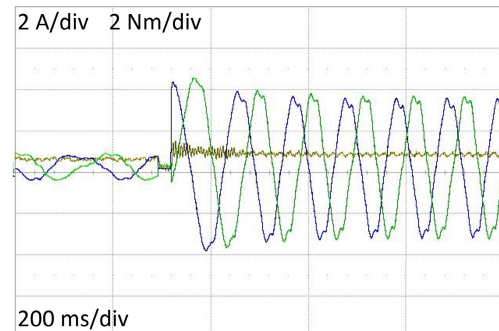
(b)

FIGURE 21. Measured current and torque transients: (a) transition from mode I to mode III and (b) from mode II to mode IV.

resistive loading were adjusted for mode II before the transition, and the current in mode I was reduced. After the transition, the flux linkage decreased, and the machine could be operated at its rated load again. The same strategy is shown in Fig. 21(b).

Finally, the torque–speed and power–speed capability curves were plotted based on the experimental results, as shown in Fig. 22. The rated powers were 161.38, 179.72, 168.06, and 185.95 W in modes I–IV, respectively. The rated speeds were 300, 592, 1103, and 2242 rpm, respectively, in modes I–IV. From this figure, we can observe that the machine could not achieve constant-power operation; hence, it is suitable for multi-speed applications such as blenders, tools, and conveyors.

A comparison of the experimental results with the simulation results is presented in Table 3. The experimental results are consistent with those of the simulations, thus confirming the flux weakening using the proposed winding switching scheme. Moreover, Figs. 18(a)–(c) and 21(a)–(b) show the feasibility of the on-line winding reconfiguration. However, for high-power applications, a more detailed transient analysis should be performed to avoid damage to the machine windings and/or power electronics.

VI. PERFORMANCE COMPARISON OF WINDING SWITCHING METHODS

A performance comparison of different winding switching methods reported in the past five years is listed in Table 4.

The proposed method has an advantage in terms of flux weakening compared with the other methods. Although it
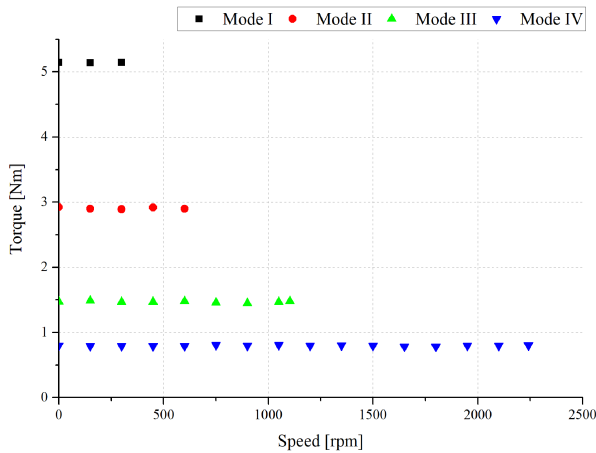
FIGURE 22. Measured speed–torque capability curves of the machine.

TABLE 3. Comparison of the simulation results and the experimental results.

Parameter	Simulation results	Experimental results
Back EMF weakening	1/1.73/3.73/6.47	1/1.74/3.67/6.49
Torque weakening	1/1.77/3.51/6.59	1/1.77/3.53/6.49
Rated speed [rpm]	300/586/1110/2208	300/592/1103/2242
Rated power [W]	162.37	161.38
Rated line voltage [V_{rms}]	43.61	58.26

TABLE 4. Performance comparison of recently reported winding switching methods.

Winding switching method	Inverter topology	Number of additional switches	Field-weakening ratios K in different operation modes
Switching method in [18]	Six H-bridge inverters	9	**1/1.03/1.41/3.86**
Cumulative/differential switching for double inverter [14]–[17], [19]	Double inverter	2	**1/3.73**
Cumulative/differential switching for single [20]	Single inverter	6	**1/3.67**
Proposed winding switching method	Single inverter	12	**1/1.74/3.67/6.49**

utilizes the highest number of additional switches, the implementation of the single inverter still imparts an advantage in favor of the proposed method over the methods presented in [14]–[19] in terms of cost. Notably, the cumulative/differential switching method for a dual inverter can utilize the voltage boost technique, which increases the available voltage by 1.73 times [16]. Therefore, this method demonstrates approximately the same performance as the proposed winding switching method in terms of the maximal achieved speed.

Notably, all the recent methods demonstrate increased back EMF total harmonic distortion in high-speed modes compared with the conventional methods [7]–[12]. This will result in an increased vibration level and power losses.

VII. CONCLUSION

This paper proposed a multi-mode operation method using winding switching, which realized the multi-speed operation of SPMSMs. Four modes of operation were achieved by combining the cumulative/differential and wye/delta switching methods. The vector summation of the back EMFs of individual coils in each mode resulted in different net back EMFs. The simulation and experimental results showed that the back EMF in the stator windings could be suppressed using only the switching winding configurations by 1.74, 3.67, and 6.49 times, respectively, compared with that in mode I. The line-to-line impedances also changed. Moreover, it was shown that the base speed increased from 1 to 1.97, 3.68, and 7.47 pu in modes I–IV, respectively, and could be further increased by applying a negative I_d current to the machine. This multi-speed operation method allows the machine to operate over a wide range of speeds, and it can be used in discrete-type applications, such as blenders and tools.

A comparison with the recently reported switching methods showed that the proposed method has both a high field-weakening ratio and low IGBT count.

REFERENCES

[1] T. Sebastiangordon and G. R. Slemon, "Operating limits of inverter-driven permanent magnet motor drives," *IEEE Trans. Ind. Appl.*, vol. IA-23, no. 2, pp. 327–333, Mar. 1987.

[2] A. M. El-Refaie and T. M. Jahns, "Optimal flux weakening in surface PM machines using fractional-slot concentrated windings," *IEEE Trans. Ind. Appl.*, vol. 41, no. 3, pp. 790–800, May/Jun. 2005.

[3] A. M. El-Refaie, T. M. Jahns, P. J. McCleer, and J. W. McKeever, "Experimental verification of optimal flux weakening in surface PM machines using concentrated windings," *IEEE Trans. Ind. Appl.*, vol. 42, no. 2, pp. 443–453, Mar./Apr. 2006.

[4] K. Atallah, D. Howe, P. H. Mellor, and D. A. Stone, "Rotor loss in permanent magnet brushless AC machines," in *Proc. IEEE Int. Electr. Mach. Drives Conf. (IEMDC)*, Seattle, WA, USA, May 1999, pp. 60–62, doi: 10.1109/IEMDC.1999.769027.

[5] Z. Q. Zhu, D. Ishak, D. Howe, and J. Chen, "Unbalanced magnetic forces in permanent-magnet brushless machines with diametrically asymmetric phase windings," *IEEE Trans. Ind. Appl.*, vol. 43, no. 6, pp. 1544–1553, Nov./Dec. 2007.

[6] R. F. Schiferl and T. A. Lipo, "Power capability of salient pole permanent magnet synchronous motors in variable speed drive applications," *IEEE Trans. Ind. Appl.*, vol. 26, no. 1, pp. 115–123, Jan./Feb. 1990.

[7] H. Huang and L. Chang, "Electrical two-speed propulsion by motor winding switching and its control strategies for electric vehicles," *IEEE Trans. Veh. Technol.*, vol. 48, no. 2, pp. 607–618, Mar. 1999.

[8] M. Ayub, S. Atiq, G. J. Sirewal, and B.-I. Kwon, "Fault-tolerant operation of wound field synchronous machine using coil switching," *IEEE Access*, vol. 7, pp. 67130–67138, 2019.

[9] M. Wang, N. Hsu, C. Chiang, S. Wang, and T. Shau, "A novel changeover technique for variable-winding brushless DC motor drives," in *Proc. SICE Annu. Conf.*, Taipei, Taiwan, 2010, pp. 2650–2653.

[10] F. Copt, D. M. Araujo, C. Koechli, and Y. Perriard, "Current control strategy for dynamic winding reconfiguration of slotless brushless DC motors," *IEEE Trans. Ind. Appl.*, vol. 55, no. 1, pp. 417–425, Jan./Feb. 2019, doi: 10.1109/TIA.2018.2869102.

[11] T. Kume and M. Swamy, "A quick transition electronic winding changeover technique for extended speed ranges," in *Proc. IEEE 35th Annu. Power Electron. Spec. Conf.*, Aachen, Germany, Jun. 2004, pp. 3384–3389.

[12] M. M. Swamy, T. Kume, A. Maemura, and S. Morimoto, "Extended high-speed operation via electronic winding-change method for AC motors," *IEEE Trans. Ind. Appl.*, vol. 42, no. 3, pp. 742–752, May/Jun. 2006.

[13] A. D. Aliabad and M. Mirsalim, "Analytic modelling and dynamic analysis of pole-changing line-start permanent-magnet motors," *IET Electr. Power Appl.*, vol. 6, no. 3, pp. 149–155, Mar. 2012.

[14] S. Hemmati and T. A. Lipo, "Field weakening of a surface-mounted permanent magnet motor by winding switching," *Electr. Power Compon. Syst.*, vol. 41, no. 13, pp. 1213–1222, Oct. 2013.

[15] S. Atiq, B.-I. Kwon, and T. A. Lipo, "Experimental verification of winding switching technique to enhance maximum speed operation of surface mounted permanent magnet machines," *IET Electr. Power Appl.*, vol. 10, no. 4, pp. 294–303, Apr. 2016.

[16] S. Atiq, T. A. Lipo, and B.-I. Kwon, "Wide speed range operation of non-salient PM machines," *IEEE Trans. Energy Convers.*, vol. 31, no. 3, pp. 1179–1191, Sep. 2016.

[17] A. Arif, N. Baloch, and B. I. Kwon, "Wide speed range operation of permanent magnet Vernier machines," *Electron. Lett.*, vol. 54, no. 18, pp. 1070–1072, Sep. 2018.

[18] H. Hijikata, Y. Sakai, K. Akatsu, Y. Miyama, H. Arita, and A. Daikoku, "Wide speed range operation by low-voltage inverter-fed MATRIX motor for automobile traction motor," *IEEE Trans. Power Electron.*, vol. 33, no. 8, pp. 6887–6896, Aug. 2018.

[19] A. Arif, N. Baloch, and B.-I. Kwon, "Winding switching and turn switching in permanent magnet Vernier machines for wide speed range operation and high efficiency," *IEEE Access*, vol. 7, pp. 55344–55357, 2019.

[20] S. Sin, M. Ayub, and B.-I. Kwon, "Operation method of non-salient permanent magnet synchronous machine for extended speed range," *IEEE Access*, vol. 8, pp. 105922–105935, 2020.

[21] M. Tian, X. Wang, D. Wang, W. Zhao, and C. Li, "A novel line-start permanent magnet synchronous motor with 6/8 pole changing stator winding," *IEEE Trans. Energy Convers.*, vol. 33, no. 3, pp. 1164–1174, Sep. 2018.

[22] W. Zhao, M. Tian, X. Wang, and Y. Sun, "Analysis of the synchronization process and the synchronization capability for a novel 6/8-pole changing LSPMSM," *IEEE Trans. Magn.*, vol. 56, no. 2, pp. 1–6, Feb. 2020.

[23] J. R. Hendershot and T. J. E. Miller, "Sinewave and squarewave motors," in *Design of Brushless Permanent-Magnet Machines*, 2nd ed. Venice, FL, USA: Motor Design Books LLC, 2010, pp. 130–131.

[24] J. R. Hendershot and T. J. E. Miller, "The circle and ellipse diagrams," in *Design of Brushless Permanent-Magnet Machines*, 2nd ed. Venice, FL, USA: Motor Design Books LLC, 2010, pp. 338–349.

STANISLAV SIN was born in 1994. He received the B.S. degree in electronics engineering from the Ferghana Polytechnic Institute, Ferghana, Uzbekistan, in 2016. He is currently pursuing the M.S. degree with the Department of Electrical and Electronic Engineering, Hanyang University, Ansan, South Korea. His research interests include electric machine control and power electronics.

MUHAMMAD AYUB was born in Quetta, Pakistan. He received the B.S. degree from the Balochistan University of Information Technology, Engineering and Management Sciences (BUITEMS), Quetta, in 2008. He is currently pursuing the Ph.D. degree with the Department of Electrical and Electronic Engineering, Hanyang University, Ansan, South Korea. He worked as a Lecturer at BUITEMS, Quetta. His research interest includes electric machine design and control.

BYUNG-IL KWON (Senior Member, IEEE) was born in 1956. He received the B.S. and M.S. degrees in electrical engineering from Hanyang University, Ansan, South Korea, in 1981 and 1983, respectively, and the Ph.D. degree in electrical engineering, machine analysis from the University of Tokyo, Tokyo, Japan, in 1989. From 1989 to 2000, he was a Visiting Researcher with the Faculty of Science and Engineering Laboratory, University of Waseda, Tokyo, Japan. In 1990, he was a Researcher with the Toshiba System Laboratory, Yokohama, Japan. In 1991, he was a Senior Researcher with the Institute of Machinery and Materials Magnetic Train Business, Daejeon, South Korea. From 2001 to 2008, he was a Visiting Professor with the University of Wisconsin–Madison, Madison, WI, USA. He is currently a Professor with Hanyang University. His research interest includes design and control of electric machines.

• • •